HEAT-TREATMENT EFFECTS ON THE PROPERTIES OF TI MADE WITH COLD SPRAYING ADDITIVE MANUFACTURING

A pure Ti deposit with a porosity of merely 2.76% was fabricated via CSAM technology, and the effects of annealing treatment on the microstructure evolution, porosity reduction, and tensile properties of the CSAM Ti were systematically investigated.

By ZHIPO ZHAO, YIDI WANG, JIQIANG WANG, TIANYING XIONG, and XINYU CUI

Cold spraying additive manufacturing (CSAM) Ti exhibits minimal plasticity, posing a significant challenge to its broader application. Heat treatment is recognized as a potent strategy to enhance the mechanical properties of additive manufacturing parts. However, prior investigations have struggled to discern the genuine impact of heat treatment on CSAM Ti due to the high porosity in initial deposits. This study addresses this gap by fabricating CSAM Ti deposits with a low porosity of 2.76%. The effects of annealing at varies temperature on the microstructure, porosity, and mechanical properties of the deposits were studied. The results show that annealing can promote recrystallization of CSAM Ti and reduce the porosity of CSAM Ti to 0.77%. This increases the strength of CSAM Ti to 780 MPa, which even exceeds that of wrought pure Ti. Despite the low elongation of 4.67%, the CSAM Ti after suitable heat treatment can be used in fields in fields don't require high plasticity.

1 INTRODUCTION

Titanium (Ti) and its alloys possess unique mechanical and chemical properties, including high specific strength, excellent corrosion resistance and biocompatibility, rendering them promising materials in various fields such as medicine, chemical industry and so on [1, 2, 3]. However, the relatively high cost has been a primary obstacle to broader adoption [4, 5]. Conventional manufacturing techniques, such as casting [6], powder metallurgy [7], and mechanical processing [8], entail substantial material and energy losses while struggling to produce complex geometries, exemplified by orthopedic implants [9]. An effective method to overcome these challenges is fabricating Ti components from powder directly via additive manufacturing such as selective laser melting (SLM) [10], electron beam melting (EBM) [11], cold spraying additive manufacturing (CSAM) [12], among others.

Cold spraying, in contrast to conventional thermal spraying — such as arc spraying [13], flame spraying [14], plasma spraying [15], HVOF [16], and HVAF [17] — offers distinct advantages. Notably, its spraying temperature remains well below the melting point of the feedstock powder, ensuring a purely solid-state deposition process. This characteristic mitigates issues such as oxidation, phase transformation, and uncontrolled grain growth in metallic powders during spraying [18]. Additional benefits encompass: (i) high deposition efficiency with low porosity [19]; (ii) induction of compressive residual stress that inhibit coating fracture [20]; (iii) capability to readily produce substantial thicknesses, reaching up to 50 mm [21]. These advantages make CSAM a promising development direction, especially for reactive raw metals (such as Ti and its alloys). However, a primary limitation lies in the near absence of ductility in as-sprayed deposits [22]. Therefore, for the components and parts prepared by CSAM, post-treatment becomes imperative to enhance their plasticity [23].

Various post-treatments have been developed to repair the defects and improve their mechanical properties of cold sprayed deposits. Notable approaches, validated for their efficacy, encompass heat treatment [24], rolling [25, 26, 27], laser processing [28], friction stir processing [23], hot isostatic pressing [29], and so on. Of these, heat treatment stands out as the most straightforward and convenient, with negligible impact on the deposit's geometry, rendering it highly compatible with the CSAM process. However, Huang et al. [30] reported heat treatment did not significantly improve the properties of CSAM Ti deposits, a finding seemingly contradictory to general heat-treatment experiences. This discrepancy may be attributed to the high porosity (14.20%) inherent in the Ti deposits examined. To clarify this issue, this study employed Ti deposits with a substantially reduced porosity of 2.76%, thereby minimizing the impact of porosity and aiming to illuminate the genuine effects of heat treatment on the microstructure and mechanical properties of CSAM Ti deposits.

2 MATERIALS AND METHODS

2.1 Raw materials

Commercial pure Ti powder, sieved through a 325-mesh sieve, served as the raw materials. Figure 1 shows morphology (a) and particle size distribution (b) of the used commercial Ti powder in this work. The Ti powder exhibits irregular morphology with a size ranging from 15 to 60 µm. Notably, the absence of satellite powder and agglomerations contributes to enhanced deposition efficiency superior deposit quality.

2.2 Fabrication of Ti deposits and heat treatment

A cold spraying system was employed to deposit Ti powder on a steel substrate. The process parameters were as follows: Compressed nitrogen served as the acceleration gas with a pressure of 4.0 MPa and a heating temperature of 800°C. A circular de Laval type nozzle, measuring 130 mm in length, 2.0 mm in throat diameter, and 8.0 mm in outlet diameter was used for the spraying process. The resulting Ti deposit exhibited a thickness of 4.0 mm.

Following the cold spraying process, electrical discharge machining (EDM) was employed to cut metallographic samples (8.0 mm × 3.0 mm × 4.0 mm) and tensile test samples (12.5 mm × 4.5 mm × 2.0 mm, with a gauge length of 5.0 mm and a cross-sectional area of 1.4 mm × 2.0 mm). A vacuum tube furnace protected by argon gas was used to anneal the samples at different temperatures for 2 hours. The CSAM Ti deposits and samples annealed at different temperature (600°C, 800°C, 1,000°C) were noted as CS-Ti, CS-Ti-600, CS-Ti-800, CS-Ti-1000.

2.3 Microstructural characterization

The samples were embedded in epoxy resin, ground with abrasive paper (from 150 grit to 3,000 grit), and polished by diamond slurries (2 µm and 0.5 µm). A field emission scanning electron microscope

(SEM, ZEISS, ULTRA PLUS) equipped with an EBSD system was used to study the microstructure of the samples. An optical metallurgical microscope (OM, ZEISS, Axio Observer Z1) was used to analyze the microstructure of the Ti deposits. The porosity of the deposits was evaluated via image analysis.

2.4 Mechanical properties tests

A tensile test was carried out using an Instron MicroTester 5848 machine at a strain rate of 10^{-3}/s. The dimensions of tensile test samples are schematically shown in Figure 7. SEM was used to analyze the fractures of CSAM Ti samples at different condition after tensile test.

3 RESULTS AND DISCUSSION

3.1 Microstructure

Figure 2 shows the metallographic structure of CSAM Ti at various conditions. As it shown in Figure 2a, tightly bonded Ti particles with a wavy pattern are evident, a result of cumulative particle deformation during spraying. Numerous black pores at particle boundary sites originate from inadequate particle deformation. The porosity of CS-Ti is measured at 2.76% according to Figure 3. After the annealing treatment at 600°C, the metallograph of Figure 2a reveals cleaner and more distinct particle boundary outlines, accompanied by the disappearance of select micropores. Nonetheless, the deformed particle boundary features persist. Elevating the annealing temperature to 800°C leads to the vanishment of these boundary characteristics, as depicted in Figure 2c, where the emergence of equiaxed grains signifies recrystallization. Meanwhile, the porosity further reduces to 1.38%, leaving predominantly larger pores. Further increasing the annealing temperature to 1,000°C induces substantial grain growth and a porosity reduction to 0.77%. Notably, pores assume an elliptical morphology, indicative of extensive solid-state diffusion facilitating the healing of smaller pores and the transformation of larger ones into quasi-spherical shapes to minimize surface energy.

Figure 4 presents the band contrast (BC) maps, inverse pole figure (IPF) maps, and grain size distributions of cold sprayed Ti (CS-Ti) under different conditions. Severe plastic deformation during the cold spraying process induces significant residual stresses within the CS-Ti, particularly at particle boundaries, resulting in a low resolution in EBSD analysis. Despite this, the reconstructed BC map clearly shows deformed Ti particles (Figure 4a). The IPF map reveals fine grains around particle boundaries with a few larger grains corresponding to undeformed particle cores (Figure 4e). The grain size distribution indicates that approximately 90% of the grains are smaller than 7 µm (Figure 4i). After annealed at 600°C, tiny grains form around the cores of prior Ti particles, creating a satellite ring around the large cores' grains (Figure 4b-f). Compared with CS-Ti, the average grain size increased slightly from 6.78 µm to 7.55 µm (Figure 4i-g). Annealing at 800°C results in complete recrystallization, with all particles growing uniformly (Figure 4c). The average grain size increased to 10.53 µm (Figure 4k). However, core and boundary grains remain distinguishable. At 1,000°C, exceeding the β-Ti transformation temperature, the annealing process involves $\alpha \rightarrow \beta$ and $\beta \rightarrow \alpha$ phase transformations. The structure of CS-Ti-1000 is completely reconstructed, eliminating the cold spraying microstructure. The average grain size increased to 14.59 µm (Figure 4l), indicating accelerated grain growth at 1,000°C,

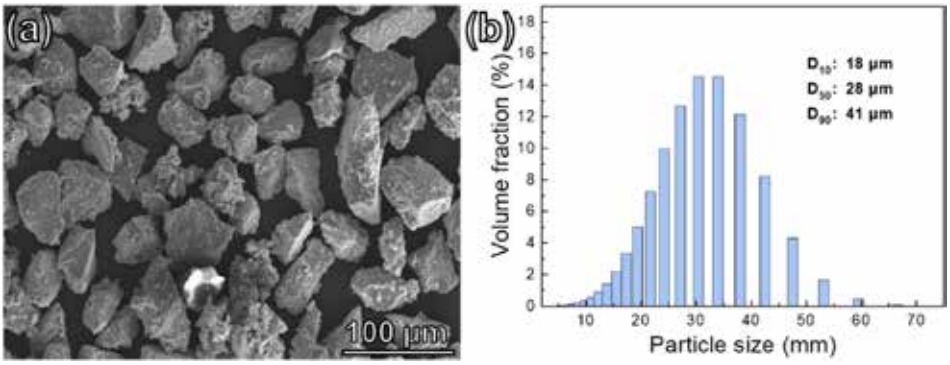

Figure 1: (a) SEM image and (b) size distribution of the commercial pure Ti powder.

Figure 2: Metallograph of CSAM Ti at various conditions: (a) CS-Ti; (b) CS-Ti-600; (c) CS-Ti-800; (d)CS-Ti-1000.

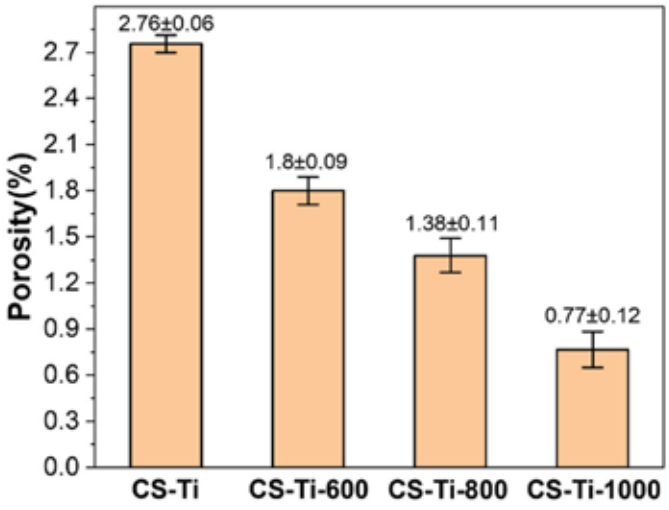

Figure 3: Porosity of CSAM Ti at different conditions.

suggesting that further increasing the annealing temperature is not advisable.

Figure 5a-d illustrate the phase maps of the samples at different conditions. The β-Ti contents for the four samples are 26.7%, 0.3%, 0, and 0.2% respectively. In CS-Ti, the β-Ti grains are small and arranged in a ring formation around the prior Ti particles. The β-Ti formation may be attributed to the severe deformation and localized temperature elevation during the impact moment. Consequently, during annealing at 600°C, most β-Ti transforms into stable α-Ti. By the time the annealing temperature reaches 800°C, β-Ti has already disappeared. The reappearance of a minor amount of β-Ti in the CS-Ti-1000 sample could be due to insufficiently slow cooling rate during annealing. Figure 5e-h shows the (geometrically necessary dislocation) GND maps of the samples. It is evident that the substantial amount of GNDs introduced during spraying were largely eliminated by 800°C annealing. As for the CS-Ti-1000, high-density GNDs sporadically distributed between grains correlate significantly with pore defects and newly formed β-Ti grains. Figure 6 shows the GND curves of CSAM Ti, clearly indicating that, as the annealing temperature gradually increases, the GND curve shifts toward lower values. The

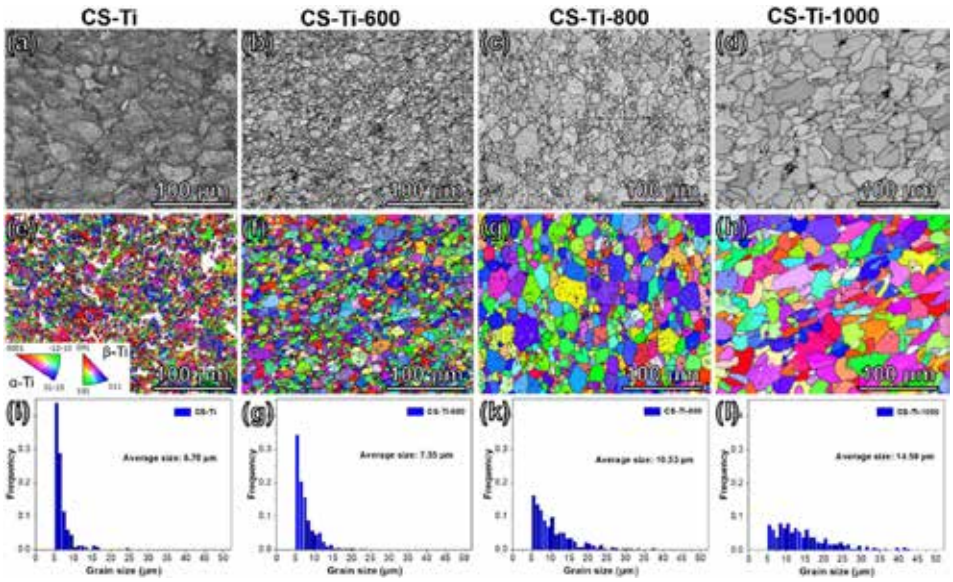

Figure 4: BC maps (band contrast), IPF (inverse polo figure) maps, and grain size distribution curves of CSAM Ti at different conditions.

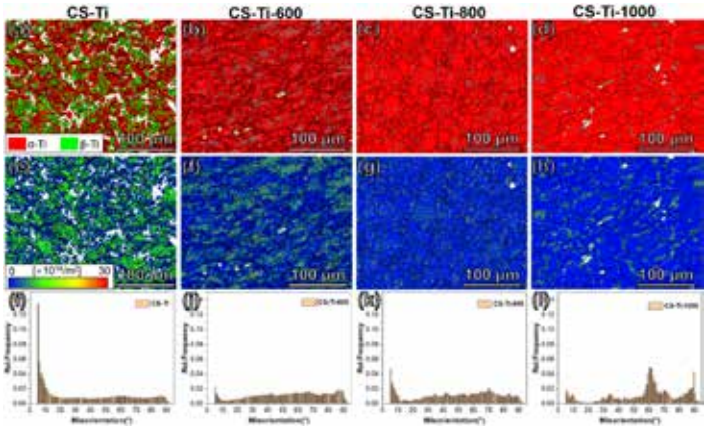

Figure 5: Phase maps, GND (geometrically necessary dislocation) maps and disorientation angle distribution of CSAM Ti at different conditions.

average GND value decreases from 11.4 × $10^{14}m^{-2}$ in CS-Ti to 1.64 × $10^{14}m^{-2}$ in CS-Ti-1000. The disorientation angle distribution in Figure 5i-l reveals some microstructure of the samples at different conditions. The high proportion of small angle disorientations in CS-Ti indicates its internal structure predominantly consists of deformed grains. As the annealing temperature rises, the proportion of low angle disorientation significantly decreases. There are three peaks in the misorientation angles (9.48°, 60°, and 90°) of α-Ti-1000, which result from the Burgers Orientation [31].

3.2 Mechanical properties

The engineering stress-strain curves of CSAM Ti at different condition is shown in Figure 7. Initially, the CS-Ti has a tensile strength of only 346 MPa and a minimal elongation of only 0.25%. Annealing at 600°C enhances the tensile strength to 512 MPa and the elongation to 0.92%. Further annealing at 800°C raises the tensile strength to 661 MPa and elongation to 2.53%, while annealing at 1,000°C results in a tensile strength of 780 MPa and a significant elongation of 4.67%. These results indicate annealing substantially improves both the strength and ductility of CSAM-Ti, with tensile strength increasing by 125% and elongation by a factor of 17.68 post-annealing. Comparatively, commercial pure Ti plate prepared by traditional rolling possess a tensile strength of 420 MPa and an elongation of 42% [30]. Although CS-Ti annealed at 1,000°C surpasses pure Ti in tensile strength, its elongation remains considerably lower, primarily due to intrinsic porosity within CSAM Ti. Despite the porosity being reduced to less than 1% in CS-Ti-1000, the presence of pores can still lead to premature failure during deformation. As depicted in Figure 8, there exists an inverse correlation between porosity and both tensile strength and elongation for CSAM Ti. The elimination of porosity through methods such as hot isostatic pressing or additional rolling could potentially augment its mechanical properties. Nonetheless, considering the economic viability and simplicity of a single heat treatment, with its elevated post-treatment strength, can feasibly substitute for wrought Ti in applications where extreme toughness is not a primary concern.

3.3 Fracture morphology

Figure 9 illustrates the fracture morphologies of CSAM Ti at different conditions after tensile test. A notable presence of pores is evident on the fracture surface of CS-Ti, as highlighted by the white arrow in Figure 9a. In the higher magnification fracture image, these pores can be seen more clearly as unbonded areas during cold spraying process (Figure 9e). Since the bonding mechanism of powder particles in cold spraying are primarily reliant on cold deformation and mechanical interlocking, it allows for the distinction of original titanium particle boundaries, outlined in yellow dotted lines in Figure 9e. Persistent porosity is observed across the entire fracture surface of the CS-Ti-600 specimen. Nevertheless, an increase in surface roughness compared to CS-Ti signifies enhanced particle cohesion. While particle outlines remain discernible at sites indicated by yellow dotted lines in Figure 9f, evidence of intergranular cleavage fracture emerges, contributing to the improved tensile strength of this sample. In the overall fracture images of CS-Ti-800 and CS-Ti-1000 samples, some wavy tear marks are found, proving the improvement of toughness of the samples. Specifically, CS-Ti-800 displays a mixed fracture mode characterized by shallow dimples (yellow arrows) alongside brittle fracture features like tear ridges (red ovals), suggesting a combination of ductile and brittle mechanisms. Conversely, CS-Ti-1000 showcases a dense array of uniform dimples, signifying superior plasticity among the tested samples. However, compared with the fine and dense deep dimples in the forged pure Ti, the dimples in CS-Ti-1000 are larger in size and shallower in depth, indicating its toughness is far from reaching the level of wrought pure Ti [32]. This is still a difficult problem that needs to be overcome in CSAM Ti.

3.4 Discussion

Based on the earlier results, it can be inferred that the effects of heat treatment on the microstructure of the CSAM Ti deposits can be divided into three ranges: (i) low-temperature zone, which is below the recrystallization temperature, primarily involves dislocation recovery; (ii) medium-temperature zone, where recrystallization of α-Ti occurs; and (iii) high-temperature zone, in which α-Ti→ β-Ti→ α-Ti transformation takes place during heating, holding, and cooling processes, completely reconstructing the microstructure of CSAM Ti. It can be seen that high-temperature treatment is beneficial for reducing porosity and increasing plasticity. However, the rapid grain growth at high temperatures will reduce the strength, which is unde-

sirable. In other words, sample heat treatment is difficult to obtain CSAM Ti with both good strength and ductility. If the cost allows, hot isostatic pressing (HIP) is undoubtedly the most effective way to improve the performance of CSAM Ti. However, it's unacceptable for most industrial products. To overcome this contradiction, follow-up studies will explore complex heat-treatment processes: first using high-temperature treatment to minimize porosity as much as possible, followed by cyclic annealing in the two-phase region to refine the grains, aiming to achieve a balance between strength, plasticity, and cost.

4 CONCLUSIONS

In this study, a pure Ti deposit with a porosity of merely 2.76% was fabricated via CSAM technology, and the effects of annealing treatment on the microstructure evolution, porosity reduction, and tensile properties of the CSAM Ti were systematically investigated.

The key findings include:

(1) Porosity reduction: The primary source of porosity in CSAM Ti stems from inadequately deformed particles during the spraying process. Annealing facilitates atomic diffusion and recrystallization, leading to the disappearance of smaller pores and the elliptical transformation of larger ones. Notably, annealing at 1,000°C for 2 hours reduced the porosity to 0.77%.

(2) Microstructural evolution: Annealing at 600°C initiates recrystallization at the peripheries of original Ti particles. As the temperature rises to 800°C, full recrystallization is observed, subsequently giving way to grain growth. Following annealing at 1,000°C, the average grain size attains 14.59 µm.

(3) Mechanical properties enhancement: Annealing concurrently enhances the tensile strength and ductility of CSAM Ti. Specifically, post-annealing at 1,000°C yields a tensile strength of 780 MPa, surpassing that of wrought pure Ti, albeit with an elongation of merely 4.67%, significantly trailing that of its wrought counterpart.

(4) Future directions: To reconcile the trade-off between porosity elimination and unchecked grain growth, future research will explore complex heat-treatment processes. These involve high-temperature exposures for porosity mitigation, succeeded by cyclic annealing within the two-phase domain to achieve grain refinement.

DECLARATION OF COMPETING INTEREST

The authors declare that they have no known competing financial interests or personal relationships that could have appeared to influence the work reported in this article.

ACKNOWLEDGEMENTS

The financial support of China Postdoctoral Science Foundation (No.2021M703278) and Innovation Foundation of Institute of Metals Research, Chinese Academy of Sciences (2022-PY16) are gratefully acknowledged.

REFERENCES

[1] Z. Li, Y. Sun, E.J. Lavernia, A. Shan; Mechanical behavior of ultrafine-grained Ti-6Al-4V alloy produced by severe warm rolling: the influence of starting microstructure and reduction ratio; Metall Mater Trans A, 46A (11) (2015), pp. 5047-5057.

[2] J.Y. Lek, A. Bhowmik, A.W.-Y. Tan, W. Sun, X. Song, W. Zhai, P.J. Buenconsejo, F. Li, E. Liu, Y.M. Lam, C.B. Boothroyd; Understanding the microstructural evolution of cold sprayed Ti-6Al-4V coatings on Ti-6Al-4V substrates; Appl Surf Sci, 459 (2018), pp. 492-504.

[3] D. Banerjee, J.C. Williams; Perspectives on titanium science and technology; Acta Mater, 61 (3) (2013), pp. 844-879.

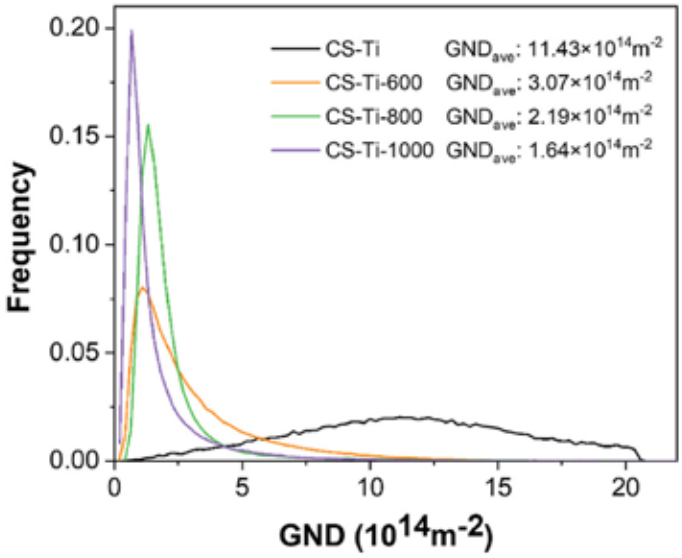

Figure 6: GND (geometrically necessary dislocation) curves of CSAM Ti at different conditions.

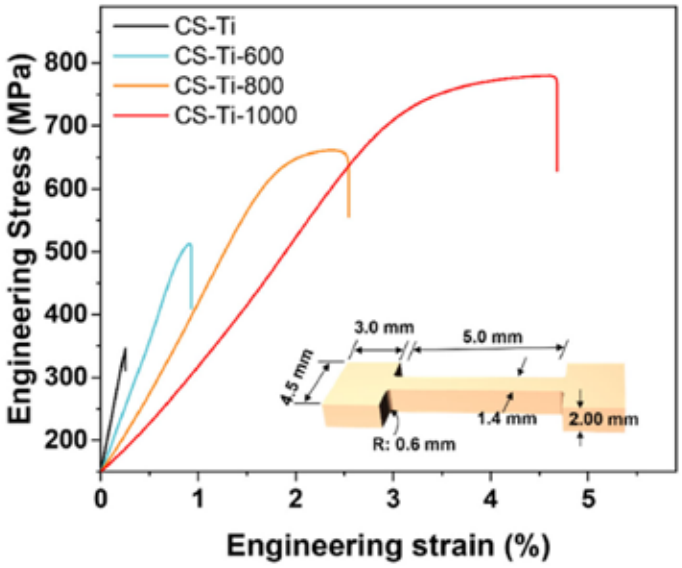

Figure 7: Engineering stress-strain curves of CSAM Ti at different condition.

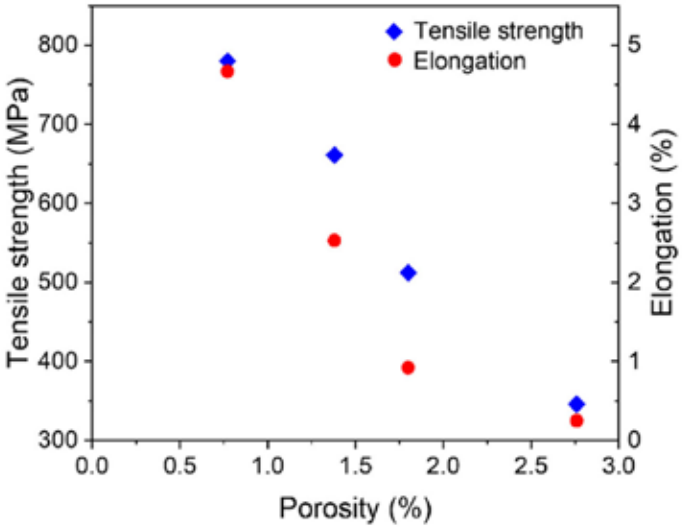

Figure 8: The relationship between porosity, tensile strength, and elongation.

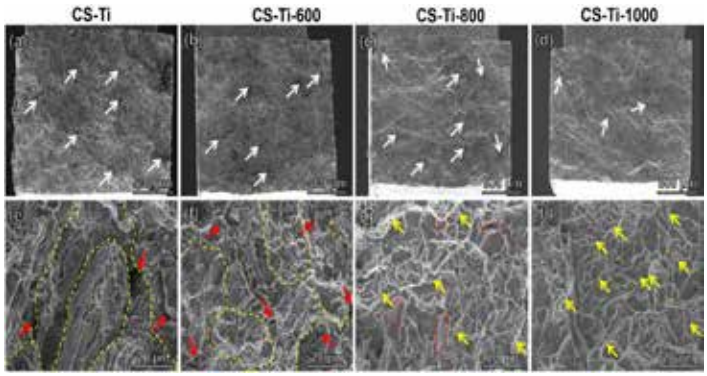

Figure 9: Fracture morphology of CSAM Ti after tensile test at different condition.

[4] J.S. Ha, S.I. Hong; Deformation and fracture of Ti/439 stainless steel clad composite at intermediate temperatures; Mater Sci Eng A Struct Mater Prop Microstruct Process, 651 (2016), pp. 805-809.

[5] H. Su, X.-b. Luo, F. Chai, J.-c. Shen, X.-j. Sun, F. Lu; Manufacturing technology and application trends of titanium clad steel plates; J Iron Steel Res Int, 22 (11) (2015), pp. 977-982.

[6] S. Ehtemam-Haghighi, K.G. Prashanth, H. Attar, A.K. Chaubey, G.H. Cao, L.C. Zhang; Evaluation of mechanical and wear properties of TixNb7Fe alloys designed for biomedical applications; Mater Des, 111 (2016), pp. 592-599.

[7] M. Karanjai, R. Sundaresan, G.V.N. Rao, T.R.R. Mohan, B.P. Kashyap; Development of titanium based biocomposite by powder metallurgy processing with in situ forming of Ca-P phases; Mater Sci Eng A Struct Mater Prop Microstruct Process, 447 (1–2) (2007), pp. 19-26.

[8] M.G. de Mello, C.A.F. Salvador, L. Fanton, R. Caram; High strength biomedical Ti–13Mo–6Sn alloy: processing routes, microstructural evolution and mechanical behavior; Mater Sci Eng, A, 764 (2019), Article 138190.

[9] H. Attar, L. Löber, A. Funk, M. Calin, L.C. Zhang, K.G. Prashanth, S. Scudino, Y.S. Zhang, J. Eckert; Mechanical behavior of porous commercially pure Ti and Ti–TiB composite materials manufactured by selective laser melting; Mater Sci Eng, A, 625 (2015), pp. 350-356.

[10] S. Liu, Y.C. Shin; Additive manufacturing of Ti6Al4V alloy: a review; Mater Des, 164 (2019).

[11] L.-C. Zhang, Y. Liu, S. Li, Y. Hao; Additive manufacturing of titanium alloys by electron beam melting: a review; Adv Eng Mater, 20 (5) (2018).

[12] S. Lett, J. Cormier, A. Quet, P. Villechaise, E. Meillot, S. Hémery; Microstructure optimization of cold sprayed Ti-6Al-4V using post-process heat treatment for improved mechanical properties; Addit Manuf, 86 (2024).

[13] Z. Yuan, Y. Jiang, Y. Lu, K. Zhang, H. Xie, Z. Ni, L. Huang, J. Liu, X. Wang, J. Peng, Z. Ling, J. Shi, P. He; Enhancing corrosion resistance of Al alloy sheets with potential gradient by arc-sprayed Zn coatings; Journal of Materials Research and Technology-Jmr&T, 33 (2024), pp. 6263-6274.

[14] P. Kumar, M.O. Jarligo, A. Asad, M. Yakout, A. McDonald; Wear and erosion performance of flame sprayed rare earth element-doped AlCoCrFeMo high entropy alloy coatings; Wear (2025), Article 205773.

[15] J. Tian, J. Zhu, J. Zheng, Y. Li, K. Yang, M. Li, H. Wang, J. He; Thermal protection mechanism of novel high-entropy rare-earth niobate coating deposited by atmospheric plasma spraying; Appl Surf Sci, 688 (2025), Article 162315.

[16] P. Junge, E.M. Heppke, R. Kleba-Ehrhardt, D. Karl, G. Cios, C. Rupprecht; Phase evolution and microstructure of suspension HVOF-sprayed alumina coatings; Surf Coating Technol, 499 (2025), Article 131885.

[17] Owoseni T.A., Baiamonte L., Dumm T., Björklund S., Joshi S.; Microstructural characteristics and wear behaviour of HVAF sprayed Ni-SiC composite coatings. Ceram Int. doi:10.1016/j.ceramint.2025.03.117 In Press.

[18] S. Yin, P. Cavaliere, B. Aldwell, R. Jenkins, H. Liao, W. Li, R. Lupoi; Cold spray additive manufacturing and repair: fundamentals and applications; Addit Manuf, 21 (2018), pp. 628-650.

[19] S.H. Zahiri, C.I. Antonio, M. Jahedi; Elimination of porosity in directly fabricated titanium via cold gas dynamic spraying; J Mater Process Technol, 209 (2) (2009), pp. 922-929.

[20] P. Sudigdo, V.S. Bhattiprolu, T. Hussain; Cold spray of Ni-based superalloys: a review on processing and residual stress; J Therm Spray Technol, 34 (2025), pp. 37-74.

[21] C. Chen, Y. Xie, S. Yin, W. Li, X. Luo, X. Xie, R. Zhao, C. Deng, J. Wang, H. Liao, M. Liu, Z. Ren; Ductile and high strength Cu fabricated by solid-state cold spray additive manufacturing; J Mater Sci Technol, 134 (2023), pp. 234-243.

[22] R. Singh, J. Kondás, C. Bauer, J. Cizek, J. Medricky, S. Csaki, J. Čupera, R. Procházka, D. Melzer, P. Konopík; Bulk-like ductility of cold spray additively manufactured copper in the as-sprayed state; Additive Manufacturing Letters, 3 (2022), Article 100052.

[23] L. Cui, W. Yang, L. Zhang, J. Hao, J. Zou, W. Zhang, L. Jia, E. Hao, J. Zhu, G. Liu; Preparation of high-tensile-ductility and high-conductivity alumina dispersion-strengthened copper via a cold spray additive manufacturing-friction stir processing composite process; J Alloys Compd, 1008 (2024), Article 176467.

[24] S. Lett, J. Cormier, A. Quet, P. Villechaise, E. Meillot, S. Hémery; Microstructure optimization of cold sprayed Ti-6Al-4V using post-process heat treatment for improved mechanical properties; Addit Manuf, 86 (2024), Article 104168.

[25] Y. Ren, N.u.H. Tariq, H. Liu, X. Cui, Y. Shen, J. Wang, T. Xiong; An innovative and flexible approach to fabricate Mg/Al composite plates: cold spraying and hot rolling post-treatment; Mater Sci Eng, A, 849 (2022), Article 143515.

[26] Z. Zhao; Formation of nanoscale interface in a high-performance TA2/Q235 clad plate; Mater Lett, 355 (2024), Article 135528.

[27] Z. Zhao, J. Tang, N.u.H. Tariq, H. Liu, H. Liu, Y. Ren, M. Tong, L. Yin, H. Du, J. Wang, T. Xiong; Effect of rolling temperature on microstructure and mechanical properties of Ti/steel clad plates fabricated by cold spraying and hot-rolling; Mater Sci Eng, A, 795 (2020), Article 139982.

[28] T. Lacondemine, B. Puga, R. Kalmar, M. Fendler, F. Balbaud; Combinatorial synthesis of AlNi alloys by low-pressure cold spray deposition and post-laser alloying process; Surf Coating Technol, 494 (2024), Article 131542.

[29] C. Chen, Y. Xie, X. Yan, S. Yin, H. Fukanuma, R. Huang, R. Zhao, J. Wang, Z. Ren, M. Liu, H. Liao; Effect of hot isostatic pressing (HIP) on microstructure and mechanical properties of Ti6Al4V alloy fabricated by cold spray additive manufacturing; Addit Manuf, 27 (2019), pp. 595-605.

[30] R. Huang, M. Sone, W. Ma, H. Fukanuma; The effects of heat treatment on the mechanical properties of cold-sprayed coatings; Surf Coating Technol, 261 (2015), pp. 278-288.

[31] C. Guo, G. Dai, J. Niu, Y. Guo, Z. Sun, H. Chang, Q. Zhang; Fe nanoparticles modified pure Ti alloy on microstructure evolution and fine crystallization mechanism fabricated by additive manufacturing; J Mater Res Technol, 26 (2023), pp. 5860-5872.

[32] L. Sun, Z. Xu, L. Peng, X. Lai; Grain-size-dependent ductile-to-brittle fracture mechanism of titanium sheets; Scr Mater, 219 (2022).

ABOUT THE AUTHOR

Zhipo Zhao, Jiqiang Wang, Tianying Xiong, and Xinyu Cui are with the Shenyang National Laboratory for Materials Science, Institute of Metal Research, Chinese Academy of Sciences. Yidi Wang is with the Shenyang National Laboratory for Materials Science, Institute of Metal Research, Chinese Academy of Sciences and the School of Materials Science and Engineering, University of Science and Technology of China.